

Physical Properties of 299 NEOs Manually Recovered in Over Five Years of NEOWISE Survey Data

Joseph R. Masiero¹, Patrice Smith^{1,2}, Lean D. Teodoro^{1,3}, A.K. Mainzer⁴, R.M. Cutri⁵, T. Grav⁴,
E. L. Wright⁶

ABSTRACT

Thermal infrared measurements of near-Earth objects provide critical data for constraining their physical properties such as size. The NEOWISE mission has been conducting an all-sky infrared survey to gather such data and improve our understanding of this population. While automated routines are employed to identify the majority of moving objects detected by NEOWISE, a subset of objects will have dynamical properties that fall outside the window detectable to these routines. Using the population of known near-Earth objects, we have conducted a manual search for detections of these objects that were previously unreported. We report 303 new epochs of observations for 299 unique near-Earth objects of which 239 have no previous physical property characterization from the NEOWISE Reactivation mission. As these objects are drawn from a list with inherent optical selection biases, the distribution of measured albedos is skewed to higher values than is seen for the diameter-selected population detected by the automated routines. These results demonstrate the importance and benefit of periodic searches of the archival NEOWISE data.

1. Introduction

Small bodies of the Solar System with perihelia less than 1.3 AU are known as near-Earth objects (NEOs). These objects are warmed by incident sunlight, and re-emit that light as thermal infrared emission, with objects that are closer to the Sun being warmer and thus brighter at infrared wavelengths. The Near-Earth Object Wide-field Infrared Survey Explorer (NEOWISE) has been carrying out a survey of the sky at thermal infrared wavelengths to detect and characterize

¹Jet Propulsion Laboratory/California Institute of Technology, 4800 Oak Grove Dr., MS 183-301, Pasadena, CA 91109, USA, *Joseph.Masiero@jpl.nasa.gov*

²University of Hawaii, Hilo, HI 96720 USA

³University of Hawaii, Manoa, HI 96822 USA

⁴University of Arizona, Tucson, AZ 85721 USA

⁵California Institute of Technology, IPAC, 1200 California Blvd, Pasadena, CA 91125 USA

⁶University of California, Los Angeles, CA, 90095

these NEOs (Mainzer *et al.* 2014a). NEOWISE began its survey on 13 December 2013 after the reactivation of the Wide-field Infrared Survey Explorer spacecraft (Wright *et al.* 2010; Mainzer *et al.* 2011a), and has continued surveying for over 6 years at $3.4\ \mu\text{m}$ and $4.6\ \mu\text{m}$ (referred to as W1 and W2, respectively). The images obtained by NEOWISE are automatically scanned for detections of moving Solar System objects, and these detections are reported regularly to the Minor Planet Center as part of regular survey data processing. Thermal modeling can be performed on these detections allowing for diameters to be constrained, as well as albedos when visible light measurements are also available, and these parameters for objects observed during the NEOWISE reactivation mission have been described in a series of papers (Mainzer *et al.* 2014a; Nugent *et al.* 2015, 2016; Masiero *et al.* 2017, 2020).

The automated WISE Moving Object Processing System (WMOPS) searches the NEOWISE data within a set of bounds that allow it to detect most, but not all, NEOs passing through the field of view. Tracklets are built from chains of detections, within set limits on acceleration, changing direction of motion, and minimum number of observations. These limits are set to maximize the number of objects identified while maintaining a reasonable number of false-positives sent for human quality assurance (cf. Cutri *et al.* 2015). These limits will, however, mean that some objects of interest will not be identified. Specifically, NEOs passing close to NEOWISE, and thus having a high rate of motion through the field of view, are less likely to meet the threshold of the minimum of 5 detections to be identified automatically. Other objects, based on viewing geometry, will exceed the allowable changes in rate and direction of motion for linking.

Because NEOWISE archives all full-frame images acquired during the survey and a database of sources detected in those images, it is possible to conduct a search for known NEOs missed by the automated processing after the fact. We present in this work a search for these objects, using the list of all currently known NEOs as of 1 June 2019 as input. A previous search to this effect was performed by Masiero *et al.* (2018), covering the first three years of the NEOWISE Reactivated survey, while Mainzer *et al.* (2014b) presented a similar search of the data from the cryogenic portion of the original WISE survey. This work uses the larger list of NEOs known presently, as well as all data from the first five and a half years of the NEOWISE Reactivation data. The aim of this search is to increase the number of NEOs with diameter and albedo characterization in order to expand our knowledge of this population, and make best use of the data obtained by the NEOWISE mission.

2. Methods

We used for our search the list of all known NEOs recorded in the Minor Planet Center’s (MPC) orbital element list MPCORB¹ as of June 1, 2019. Using these orbital elements, we determined the

¹<https://www.minorplanetcenter.net>

subset of objects that were at Solar elongations between $88^\circ - 115^\circ$ (the NEOWISE field of regard during the mission) and predicted apparent magnitudes of $V < 20$ mag during the time of the NEOWISE Reactivation survey. Each object on this list was queried from one month before to one month after the date of peak brightness in the searched elongation region using the IRSA WISE Moving Object Search Tool² through the API interface. These searches produced a list of WISE images that overlapped the predicted position of each NEO, and thus might contain a previously unidentified detection.

The images were visually inspected to look for sources coincident with the predicted positions of each object. Images without identifiable sources were removed from the list, and then the NEOWISE-R Single Exposure Source Table³ was searched for entries within $5''$ of the predicted position of each NEO at the time of the NEOWISE observation. Objects with NEOWISE observations already reported to the MPC by the automated WMOPS system were not included in this search for the epochs that had been reported. However, this search did return additional detections for previously reported NEOs at new epochs. Increasing the number of identified observing epochs for NEOs is critical for advanced thermophysical modeling work that uses multiple viewing geometries to constrain NEO surface thermal inertias (e.g. Delbo’ *et al.* 2007; Koren *et al.* 2015; Delbo *et al.* 2015; Hanuš *et al.* 2016; Masiero *et al.* 2019, etc.).

The resulting list of returned detections contained objects with as few as one detection to as many as 34 detections. For objects detected in only a single image, there is a significant potential for stars, cosmic rays, or other artifacts and noise sources to masquerade as real detections, so a second visual inspection of these detections was carried out. After this inspection, 48 NEOs with single detections were determined to have a high probability of being real, and 38 of these were detected in both NEOWISE bandpasses (which are imaged simultaneously).

Objects detected five or more times are of particular interest because they represent tracklets that could have been identified by the WMOPS automated processing routines, but were not for various reasons. The WMOPS software identifies objects by first creating pairs of detections, and then linking these pairs based on common motion vectors. The WMOPS velocity limits on creating pairs ($0.021 \text{ deg day}^{-1} < \text{velocity} < 3.22 \text{ deg day}^{-1}$) along with the acceleration tolerance ($< 0.01 \text{ deg day}^{-2}$) and angle of motion tolerance ($< 1^\circ$) used for linking them define a phase space where WMOPS can detect objects. The majority of the NEOs with five or more detections found in our manual search here are outside this phase space, as shown in Figure 1. The remaining 21 objects that are within this phase space were lost either because they were near the signal-to-noise detection limit ($S/N > 4.5$) used to compile the input list to build detection pairs, or they were in a region of sky with a dense background and so were lost during the catalog-based filtering for stationary object rejection that is done at the beginning of WMOPS processing.

²<https://irsa.ipac.caltech.edu/applications/MOST/>

³<https://irsa.ipac.caltech.edu/>

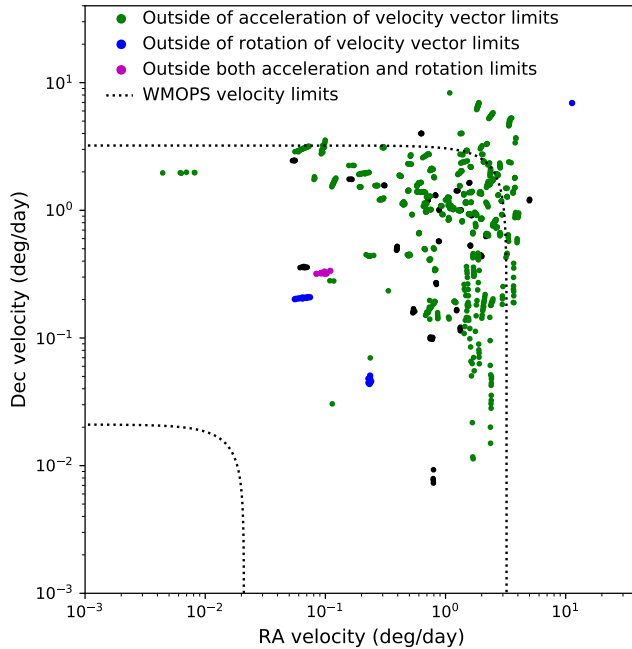


Fig. 1.— Rates of motion in RA and Dec of all objects presented here that were detected more than five times (the minimum required for automated detection). Each tracklet will be shown as a string of dots based on the changes in motion within the tracklet. Dotted lines show the lower and upper limits to rate of motion that WMOPS will detect. Green points are tracklets that had accelerations beyond the limit accepted by WMOPS; blue point had rotations in the angle of motion outside the WMOPS limit; purple points are tracklets the exceeded both limits. Black points within the WMOPS velocity limits were not found either due to falling below the detection threshold, or having detections rejected by the atlas-based stationary object rejection routines.

It is important to note that the vast majority of NEOs were discovered by ground-based visible light telescopes, and thus will have a preferential bias toward high-albedo objects at any given size range, as visible surveys are brightness-limited. This bias will combine with the selection bias we impart by looking for objects with visually bright apparitions at the time they approached the NEOWISE field of regard, resulting in our list preferentially containing more high-albedo asteroids than would be found in an unbiased sample of the true NEO population.

3. Thermal Modeling

We employed the Near-Earth Asteroid Thermal Model (NEATM, Harris *et al.* 1998) to constrain the physical properties of the detected asteroids using their NEOWISE thermal infrared mea-

surements, following the procedure used in our previous study of NEOWISE manually-recovered NEOs (Masiero *et al.* 2018). Using the tables of detections published in IRSA, we extract the W1 and W2 profile-fit photometry and astrometry for the detections of these objects. In addition to visual inspection of all detections to remove contamination from cosmic rays, artifacts, and background stars, we also performed an automated filtering on the detections before using them for thermal modeling, as described below.

Every detection published in IRSA includes a reduced χ^2 (*rchi2*) value of the fit of the PSF model to the presumed source in each bandpass. We reject all detections with *rchi2* > 20, as this indicates a high likelihood of a contaminated detection. In general, values of *rchi2* > 5 are removed from analysis as they have a higher likelihood of being cosmic rays (e.g. Masiero *et al.* 2020). However any source that is trailed, even at the sub-PSF level, may have an increased *rchi2* value and so for this work we only reject sources with *rchi2* > 20 to remove the most serious cosmic ray contamination. This cut was determined through visual validation of the detections of singleton objects that were slightly trailed and seen in both bands, providing a guide for what the largest acceptable *rchi2* would be for this work.

We also reject 2-band detections where $W1 - W2 < 1$ mag to remove contamination from stars. During initial thermal modeling tests, we found instances of detections contaminated by comparably bright stars, which created problems for the thermal model fitting. The majority of stars are in the Rayleigh-Jeans portion of their spectral energy distribution at the W1 and W2 wavelengths, so the expected W1-W2 color is ~ 0 , while for sources with rising thermal emission in W2, such as asteroids inside ~ 3 AU, this color is expected to be redder. An analysis of the W1-W2 colors of all sources detected in two bands shows a peak of the distribution at $W1 - W2 \sim 2.6$ mag, with the vast majority of sources within 1.5 mag of that peak. Visual inspection of sources with $W1 - W2 < 1$ mag confirmed the predicted positions coincide with stationary background objects, so this color is used as a cut on the data prior to thermal modeling. In total, 40 detections (out of 1688) were eliminated from fitting by color and *rchi2* cuts. This cut would also reject distant asteroids dominated by reflected light in the W1 and W2 bands, however these are highly unlikely to have large rates of motion and be missed by WMOPS, if bright enough to be detected.

Proximity of the asteroid to the WISE spacecraft is the main reason that objects will be moving too fast or accelerating too much to be detected often enough for automated identification. As NEOWISE observes at a narrow range of Solar elongations, observer distance and observational phase angle are coupled. This results in the detections presented here being made at higher phase angles than NEOs discussed in previous work (Nugent *et al.* 2015, 2016; Masiero *et al.* 2017). The NEATM beaming parameter, used to account for model uncertainties, is correlated with phase (Mainzer *et al.* 2011b), and as such we assume a larger beaming parameter here than is used for other studies of NEOWISE-observed NEOs. Following Masiero *et al.* (2018) we assume model beaming parameters of $\eta = 2.0 \pm 0.5$. We also assume ratios of the infrared albedo at $3.4 \mu\text{m}$ (p_{IR}) to the visual albedo of $p_{IR}/p_V = 1.6 \pm 1.0$. The uncertainties on these parameters are fed into our Monte Carlo analysis to determine overall diameter uncertainty.

We employ a Monte Carlo analysis of our fit to constrain the statistical uncertainty on our diameter determinations. Taking the uncertainties on our measured parameters as well as the assumed uncertainty on our fixed model parameters as discussed above, we vary each input to our model over 25 iterations and use the resultant spread of the diameters and albedos in the model solutions as the quoted uncertainty on our best-fit values. For the $W1$ and $W2$ magnitudes, measurement uncertainties are taken from the Single-Exposure Source Table. For the measured H magnitude, we assume an uncertainty of 0.2 magnitudes following previous work (e.g. Masiero *et al.* 2018), as no uncertainty is provided in the MPC catalog. We assume all parameters can be modeled by a Gaussian distribution, with the uncertainties giving the 1σ value and the measured/assumed value as the mean of the distribution. We note that for the flux uncertainties specifically, Wright *et al.* (2018) showed that while they are not strictly Gaussian, the actual measurement uncertainty can be encompassed by a Gaussian using the published value. Thus, this assumption is sufficient for our analysis where the fit uncertainties are dominated by other terms, such as the unknown beaming parameter.

In addition to statistical uncertainties on the thermal model fits, there are also systematic model uncertainties to consider. NEATM is an imperfect model that assumes the night side of an asteroid contributes no thermal emission. While this will only have a small effect on objects at low phase angles, at higher phases this results in an underestimation of the emitted flux and an overestimation of the diameter. Mommert *et al.* (2018) showed that beyond a phase angle of $\alpha > 65^\circ$ NEATM deviates from the true diameter, and requires a correction factor to accurately reproduce input thermophysical model parameters. The objects in our sample have a mean phase angle of $\alpha = 73^\circ$, and three-quarters of them were seen at phases beyond $\alpha = 65^\circ$. In light of this, we also calculated the corrected diameters and albedos based on the correction equations from Mommert *et al.* (2018). However we note that this correction was developed from a NEATM model fit to multiple wavelengths spanning the peak of thermal emission, and so may not completely correct for the model offsets in our implementation of NEATM.

A further source of uncertainty for the fits presented in this work is the unknown light curve phase for objects with a small number of detections. As discussed in Mainzer *et al.* (2014b) and Masiero *et al.* (2018), when an object has only a few samplings of its light curve available, the error on determining the mean of the light curve (which enables fitting an effective spherical diameter for a body) increases, up to $\sim 30\%$ of the light curve amplitude for a single detection. For an object with a light curve amplitude of > 1 mag this can result in an offset of the fitted diameter from the true spherical equivalent diameter of $> 15\%$. In addition to this effect, light curve variations as well as the Eddington bias can result in objects near the detection limit having overestimated fluxes, artificially increasing the fitted diameter compared to the true size. For the objects presented here, our median S/N in $W2$ was larger than 10, so this will not have a significant impact on these fits, but should be kept in mind when dealing with objects with a small number of detections.

4. Results and Discussion

The results of our modeling, including the best fit values and Monte Carlo error analyses, are presented in Table 1. We describe 303 NEATM fits of 299 unique near-Earth objects, of which 239 had not been previously characterized by the reactivated NEOWISE mission. The remaining 60 objects had been detected and reported by the spacecraft at a different observing epoch since the reactivation in Dec 2013. The four objects with multiple fits show good agreement within the quoted statistical uncertainties from the Monte Carlo analysis. For all objects and epochs, the measured astrometry data have been reported to the MPC, and are archived there.

Previous work has shown that fits of objects with reflected light contributions to the $W2$ band above 10% of the total flux are less-reliable (cf. Masiero *et al.* 2017), and thus we removed from our physical property list fits of 19 objects that were detected by NEOWISE but fell in this regime. These objects were: (152952),(163132),(163243),(281375),(304640),(364136),(388945), (418198), (472263), (530743), (536531), 2009 FU23, 2017 OO1, 2017 RV17, 2017 VX1, 2017 VW13, 2018 RP8, 2018 UY, 2019 CE. The astrometry for these objects recovered in our search were still submitted to the MPC.

We show in Figure 2 a comparison of the diameters and albedos for the objects presented here, along with those published from our previous manual recovery search (Masiero *et al.* 2018) and the fits for objects found by our automated WMOPS detection algorithms. As expected, the bias in favor of high albedo objects (due to the initial discovery selection effect combined with the selection effect on the input list for our search) is clearly apparent in the distribution of our sample, with the majority of objects having fits in the with albedos greater than $p_V > 0.1$. This work recovered more large objects than our previous manual search, with 78 objects having fitted diameters larger than 1 km. This is because our new search included all objects in the NEO orbital list, while our previous work focused on short-arc asteroids that had been discovered more recently. More recently discovered objects tend to be smaller as there are fewer large objects remaining undiscovered as the global NEO survey programs progress.

We can use the 60 objects that have previously reported NEOWISE-Reactivation diameters to verify the accuracy of the model results presented here. We show in Figure 3 the comparison of the diameters presented in this paper to those previously published values. The diameters in this work show a fairly large random scatter, as well as a systematic offset to larger values. This is likely due to a combination of effects including the smaller number of detections which present a bias toward light curve maxima, as well as the larger phase angles of observation which are detrimental to the NEATM fitting accuracy. Although we include the correction to the NEATM fits proposed by Mommert *et al.* (2018), which provides a small improvement to this offset, it does not fully eliminate it.

We can also compare our physical property results to those NEOs with sizes measured by the Spitzer space telescope (Trilling *et al.* 2016). The objects targeted by Spitzer are generally are smaller than those regularly detected by the NEOWISE automated pipeline, but our manual

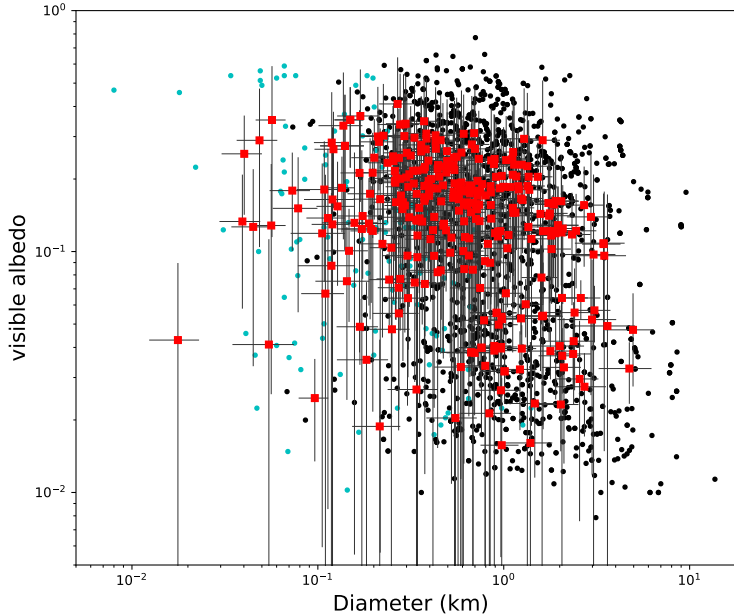


Fig. 2.— Diameters and albedos for near-Earth objects presented here (red squares), compared with manually detected NEOs presented in Masiero *et al.* (2018) (cyan dots) and NEOs detected automatically in the first five years of the NEOWISE Reactivation survey (black dots). Error bars are shown only for the newly presented objects, but are comparable in size for all fits. The search criteria used here that targets objects with predicted visual magnitudes brighter than $V=20$ mag at the time they passed through the NEOWISE field of regard, combined with the preferential discovery of high albedo objects by optical telescopes, results in a significant bias against low albedo NEOs.

recovery allows us to find more objects in this smaller size range. We extracted all NEOs with Spitzer CH2 $S/N > 5$ from the online database of fitted properties⁴. There are 105 objects from there in common with our table of fitted properties. A comparison between the sizes published in these two data sets is shown in Figure 4.

The fits presented here here tend to be somewhat larger than those derived from the Spitzer data, though not as large as the offset from previous NEOWISE epochs. Due to the limited time window over which Spitzer observed most NEOs, those data may show some of the same effects and biases associated with limited lightcurve sampling as our fits, however this effect will be more pronounced for objects seen by NEOWISE in a small number of short exposures. Additionally, the

⁴<http://nearearthobjects.nau.edu>

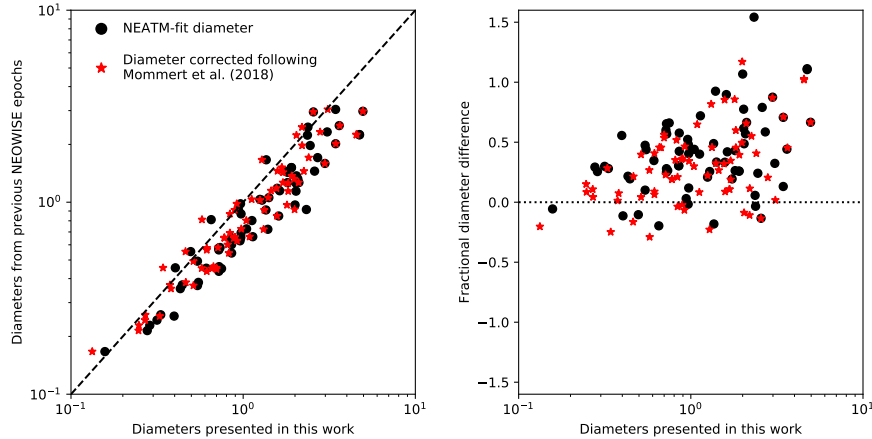


Fig. 3.— Comparison of the diameters presented in this work to previously-published NEOWISE diameters of the same NEOs at different observing epochs (left). Fits from the NEATM model are shown as black circles, and sizes corrected following (Mommert *et al.* 2018) are shown as red stars. The fractional difference between these fits (right) shows that the NEATM fits to the higher phase angle data tends to over-estimate the sizes compared to previous work.

larger beaming parameter used for our fits (due to the typically higher phase angle of observation) also will skew the fits to a larger size.

Given the results of these comparisons, the diameters presented here may be over-estimates of the actual spherical equivalent diameter. This highlights the limitations of NEATM as well as the need to use thermophysical models for objects with high phase angle observations to more accurately constrain sizes. Performing thermophysical modeling on the NEOWISE and Spitzer observations together would further enhance the benefits of this technique.

5. Conclusions

We present diameter fits for 299 NEOs found through manual searches of the NEOWISE data archive, 239 of which had no previously reported NEOWISE-derived diameter. Due to the detection circumstances of these objects, and the larger phase angles at which they are observed compared to the automatically-detected objects, the uncertainty on the diameter determination is larger, and there is a systematic offset in the fitted diameters to larger sizes in this work. Thus, the diameters presented in many cases represent over-estimates of the true effective spherical diameter of these bodies. These observations, however, do provide some constraint on the overall size of these NEOs, and are important additions to the multiple observing epochs needed to carry out more advanced thermophysical modeling.

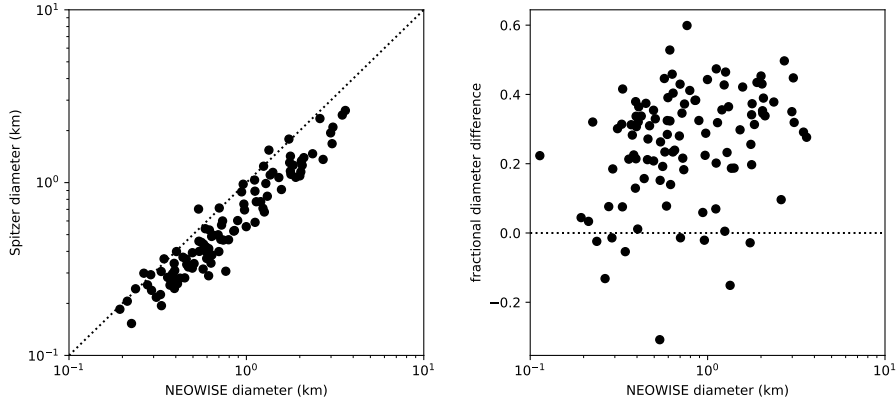


Fig. 4.— Comparison of NEO diameters presented here to sizes determined by Spitzer (left) and fractional diameter difference between the two data sets (right). Sizes derived here are larger than those found by Spitzer by $\sim 30\%$, which is a result of the larger assumed beaming parameter chosen here.

When combined with all previous publications, the diameters presented here bring the total number of NEOs characterized by the NEOWISE-Reactivation mission to 1193 since the survey was restarted in Dec 2013. Combined with objects observed during the initial WISE mission phases before hibernation, a total of 1652 NEOs have physical property characterization using data from the WISE and NEOWISE missions. As NEOs continue to be discovered by ongoing and future surveys, the archived NEOWISE single-frame images will be an important resource for recovering characterization data well after the mission has ended. The NEOWISE data are already an important legacy data set with a large amount of information not currently known that is waiting to be revealed.

Acknowledgments

The research was carried out at the Jet Propulsion Laboratory, California Institute of Technology, under a contract with the National Aeronautics and Space Administration (80NM0018D004). This publication makes use of data products from the Wide-field Infrared Survey Explorer, which is a joint project of the University of California, Los Angeles, and the Jet Propulsion Laboratory/California Institute of Technology, funded by the National Aeronautics and Space Administration. This publication also makes use of data products from NEOWISE, which is a joint project of the University of Arizona and Jet Propulsion Laboratory/California Institute of Technology, funded by the Planetary Science Division of the National Aeronautics and Space Administration. This research has made use of data and services provided by the International Astronomical Union’s Minor Planet Center. This research has made use of the NASA/IPAC Infrared Science Archive,

which is operated by the California Institute of Technology, under contract with the National Aeronautics and Space Administration. This research has made extensive use of the *numpy*, *scipy* (Virtanen *et al.* 2020), *astropy* (Astropy Collaboration *et al.* 2013, 2018), and *matplotlib* Python packages.

REFERENCES

- Astropy Collaboration, Robitaille, T. P., Tollerud, E. J., *et al.*, 2013, A&A, 558, A33.
- Astropy Collaboration, Price-Whelan, A. M., Sipőcz, B. M., *et al.*, 2018, AJ, 156, 123.
- Cutri, R.M., Mainzer, A., Conrow, T., Masci, F., Bauer, J., *et al.*, 2015, Explanatory Supplement to the NEOWISE Data Release Products, <https://wise2.ipac.caltech.edu/docs/release/neowise/expsup>
- Delbo', M., dell'Oro, A., Harris, A.W., Mottola, S., & Mueller, M., 2007, Icarus, 190, 236.
- Delbo', M., Mueller, M., Emery, J.P., Rozitis, B., & Capria, M.T., 2015, Asteroids IV (P. Michel, F. DeMeo, W.F. Bottke eds), University of Arizona Press, 107.
- Hanuš, J., Delbo', M., Vokrouhlický, D., 2016, A&A, 592, 34.
- Harris, A.W., 1998, Icarus, 131, 291.
- Koren, S.C., Wright, E.L. & Mainzer, A.K., 2015, Icarus, 258, 82.
- Mainzer, A.K., Bauer, J.M., Grav, T., Masiero, J., *et al.*, 2011a, ApJ, 731, 53.
- Mainzer, A.K., Grav, T., Bauer, J.M., Masiero, J., *et al.*, 2011b, ApJ, 743, 156.
- Mainzer, A.K., Bauer, J., Cutri, R., Grav, T., Masiero, J., *et al.*, 2014a, ApJ, 792, 30.
- Mainzer, A.K., Bauer, J., Grav, T., Masiero, J., Cutri, R., *et al.*, 2014b, ApJ, 784, 110.
- Masiero, J.R, Nugent, C., Mainzer, A.K., Wright, E., Bauer, J., *et al.*, 2017, AJ, 154, 168.
- Masiero, J.R, Redwing, E., Mainzer, A.K., Bauer, J.M., Cutri, R.M., *et al.*, 2018, AJ, 156, 60.
- Masiero, J.R, Wright, E.L., & Mainzer, A.K., 2019, AJ, 158, 97.
- Masiero, J.R, Mainzer, A.K., Grav, T., *et al.*, 2020, PSJ, 1, 5.
- Mommert, M., Jedicke, R., & Trilling, D., 2018, AJ, 155, 74.
- Nugent, C.R., Mainzer, A., Masiero, J., Bauer, J.M., Cutri, R.M. *et al.*, 2015, ApJ, 814, 117.
- Nugent, C.R., Mainzer, A., Bauer, J.M., Cutri, R.M., Kramer, E. *et al.*, 2016, AJ, 152, 63.

Trilling, D.E., Mommert, M., Hora, J., *et al.*, 2016, *AJ*, 152, 172.

Virtanen, P., Gommers, R., Oliphant, T., *et al.*, 2020, *Nature Methods*, 17, 261.

Wright, E.L., Eisenhardt, P., Mainzer, A.K., Ressler, M.E., Cutri, R.M., *et al.*, 2010, *AJ*, 140, 1868.

Wright, E.L., Mainzer, A.K., Masiero, J., Grav, T., Cutri, R.M., Bauer, J.M., 2018, arXiv:1811.01454.

Table 1:: Thermal model fits for manually recovered NEOs detected in the NEOWISE Reactivation survey data. Names are in MPC-packed format, H and G are the input photometric parameter measurements used by the model, p_V is the visible light albedo, and n_{W1} and n_{W2} are the numbers of detections in the W1 and W2 bandpasses. D_{corr} and $p_{V_{corr}}$ have been corrected following the equations in Mommert *et al.* (2018).

[†]Albedo uncertainties are symmetric in log-space as the error is dominated by the uncertainty on H ; the asymmetric linear equivalents of the 1σ log-space uncertainties are presented here.

Name	input H (mag)	G	Diameter (km)	D_{corr} (km)	p_V^{\dagger}	$p_{V_{corr}}$	beaming	n_{W1}	n_{W2}	phase (deg)	Mean MJD days
85275	16.10	0.15	3.614 ± 1.475	3.643	0.049 (+0.123/-0.035)	0.048	2.00 ± 0.50	0	1	37.11	57329.3314
85713	15.60	0.15	3.442 ± 1.028	3.098	0.108 (+0.074/-0.044)	0.134	2.00 ± 0.50	5	5	75.50	56977.7030
85953	18.10	0.15	0.959 ± 0.207	0.922	0.122 (+0.058/-0.039)	0.134	2.00 ± 0.50	3	3	63.29	58220.0983
85989	17.10	0.15	2.986 ± 1.041	2.978	0.052 (+0.043/-0.023)	0.053	2.00 ± 0.50	13	13	49.39	56875.8718
85990	20.20	0.15	0.404 ± 0.108	0.342	0.113 (+0.069/-0.043)	0.153	2.00 ± 0.50	2	2	83.11	57023.2583
86819	17.40	0.15	1.124 ± 0.259	1.043	0.259 (+0.165/-0.101)	0.304	2.00 ± 0.50	16	17	70.67	56934.4738
88213	19.40	0.15	0.940 ± 0.249	0.893	0.050 (+0.030/-0.019)	0.056	2.00 ± 0.50	6	6	66.03	58195.2370
89959	16.40	0.15	1.903 ± 0.617	1.893	0.162 (+0.138/-0.075)	0.167	2.00 ± 0.50	6	6	50.85	58374.7789
90416	18.60	0.15	2.001 ± 0.703	1.797	0.041 (+0.034/-0.018)	0.050	2.00 ± 0.50	3	3	75.85	57071.5748
96590	16.20	0.15	1.737 ± 0.446	1.583	0.159 (+0.092/-0.058)	0.192	2.00 ± 0.50	4	4	73.58	58167.5872
99907	17.90	0.15	0.734 ± 0.181	0.714	0.243 (+0.141/-0.089)	0.263	2.00 ± 0.50	5	4	60.12	58094.0256
A3067	16.80	0.15	1.342 ± 0.323	1.266	0.187 (+0.161/-0.087)	0.214	2.00 ± 0.50	6	6	67.36	57069.8124
D6793	18.30	0.15	0.998 ± 0.270	0.984	0.186 (+0.143/-0.081)	0.195	2.00 ± 0.50	10	10	55.22	57880.0746
D6839	18.70	0.15	0.611 ± 0.157	0.574	0.157 (+0.144/-0.075)	0.180	2.00 ± 0.50	0	1	68.00	58126.7572
D6923	16.20	0.15	3.042 ± 0.946	3.066	0.097 (+0.112/-0.052)	0.096	2.00 ± 0.50	4	4	37.95	57951.2161
D7032	16.60	0.15	2.046 ± 0.552	2.040	0.120 (+0.083/-0.049)	0.123	2.00 ± 0.50	1	1	49.54	57701.1332
D7078	16.20	0.15	1.524 ± 0.304	1.455	0.204 (+0.090/-0.062)	0.229	2.00 ± 0.50	5	5	64.88	57904.7839
D7158	17.90	0.15	0.849 ± 0.167	0.776	0.187 (+0.099/-0.065)	0.225	2.00 ± 0.50	5	5	73.11	57193.0565
D7805	16.60	0.15	4.738 ± 1.497	4.546	0.033 (+0.024/-0.014)	0.036	2.00 ± 0.50	5	5	63.67	58528.2073
D7925	15.90	0.15	2.040 ± 0.495	1.914	0.162 (+0.089/-0.058)	0.187	2.00 ± 0.50	3	3	68.58	58185.7849
D8325	16.80	0.15	1.031 ± 0.249	0.961	0.240 (+0.130/-0.084)	0.279	2.00 ± 0.50	6	6	69.68	57511.6834
D8404	19.10	0.15	0.477 ± 0.090	0.392	0.131 (+0.060/-0.041)	0.187	2.00 ± 0.50	2	3	86.50	57825.5758
D8846	16.00	0.15	2.707 ± 0.734	2.401	0.156 (+0.096/-0.059)	0.197	2.00 ± 0.50	6	6	77.55	57881.6361
D8859	18.90	0.15	0.568 ± 0.175	0.514	0.191 (+0.215/-0.101)	0.233	2.00 ± 0.50	4	4	74.51	58495.2781
D9345	16.70	0.15	1.620 ± 0.388	1.489	0.290 (+0.223/-0.126)	0.345	2.00 ± 0.50	3	4	72.14	58258.4646
E0158	18.40	0.15	0.637 ± 0.141	0.603	0.155 (+0.079/-0.052)	0.176	2.00 ± 0.50	4	4	66.56	58108.6917
E0333	19.00	0.15	0.430 ± 0.108	0.381	0.287 (+0.194/-0.116)	0.362	2.00 ± 0.50	5	5	77.56	58356.2467
E1484	16.40	0.15	1.287 ± 0.292	1.253	0.294 (+0.182/-0.112)	0.317	2.00 ± 0.50	0	1	59.71	57065.4061
E1495	18.30	0.15	0.540 ± 0.135	0.476	0.245 (+0.157/-0.096)	0.313	2.00 ± 0.50	3	3	78.35	58603.3027
E1527	18.90	0.15	0.534 ± 0.153	0.466	0.167 (+0.135/-0.075)	0.217	2.00 ± 0.50	4	4	79.86	58349.8840
E1851	17.70	0.15	0.893 ± 0.186	0.843	0.242 (+0.126/-0.083)	0.277	2.00 ± 0.50	7	7	67.34	57664.8948
E3947	15.30	0.15	2.945 ± 0.760	2.870	0.139 (+0.114/-0.063)	0.150	2.00 ± 0.50	19	20	59.43	58623.9676
E4332	16.50	0.15	1.770 ± 0.437	1.529	0.144 (+0.090/-0.055)	0.190	2.00 ± 0.50	11	12	80.98	58369.3077
E4898	18.80	0.15	0.383 ± 0.092	0.377	0.309 (+0.212/-0.126)	0.327	2.00 ± 0.50	5	5	56.19	58608.4373
F2671	20.10	0.15	0.326 ± 0.068	0.311	0.216 (+0.100/-0.068)	0.242	2.00 ± 0.50	6	6	64.72	57545.9042
F2685	19.20	0.15	0.397 ± 0.091	0.331	0.170 (+0.087/-0.057)	0.238	2.00 ± 0.50	3	3	85.09	57710.6282
F3953	16.80	0.15	1.263 ± 0.229	1.211	0.164 (+0.065/-0.047)	0.182	2.00 ± 0.50	6	7	63.82	57432.4794
F4229	16.50	0.15	1.339 ± 0.387	1.160	0.226 (+0.229/-0.114)	0.297	2.00 ± 0.50	1	2	80.72	56870.7552
F4275	20.10	0.15	0.262 ± 0.054	0.215	0.193 (+0.141/-0.081)	0.276	2.00 ± 0.50	1	1	86.37	56819.3343
F4555	16.70	0.15	1.625 ± 0.450	1.564	0.122 (+0.077/-0.047)	0.134	2.00 ± 0.50	6	6	62.90	57513.8059
F5140	17.40	0.15	1.629 ± 0.406	1.453	0.054 (+0.036/-0.022)	0.068	2.00 ± 0.50	3	3	76.80	58383.3960
F9504	17.00	0.15	3.075 ± 0.674	2.800	0.057 (+0.028/-0.019)	0.069	2.00 ± 0.50	7	7	73.77	57324.0052
G1989	17.20	0.15	1.137 ± 0.244	1.089	0.229 (+0.172/-0.098)	0.255	2.00 ± 0.50	2	2	64.07	57671.2221

Table 1:: Thermal model fits for manually recovered NEOs detected in the NEOWISE Reactivation survey data. Names are in MPC-packed format, H and G are the input photometric parameter measurements used by the model, p_V is the visible light albedo, and n_{W1} and n_{W2} are the numbers of detections in the W1 and W2 bandpasses. D_{corr} and $p_{V_{corr}}$ have been corrected following the equations in Mommert *et al.* (2018).

[†]Albedo uncertainties are symmetric in log-space as the error is dominated by the uncertainty on H ; the asymmetric linear equivalents of the 1σ log-space uncertainties are presented here.

Name	input H (mag)	G	Diameter (km)	D_{corr} (km)	p_V^{\dagger}	$p_{V_{corr}}$	beaming	n_{W1}	n_{W2}	phase (deg)	Mean MJD days
G2058	17.90	0.15	1.608 ± 0.466	1.571	0.054 (+0.077/-0.032)	0.058	2.00 ± 0.50	1	1	58.57	56856.9883
G2142	18.70	0.15	0.724 ± 0.209	0.672	0.170 (+0.137/-0.076)	0.200	2.00 ± 0.50	11	11	70.64	57645.3273
G2269	17.00	0.15	1.196 ± 0.339	1.138	0.187 (+0.134/-0.078)	0.210	2.00 ± 0.50	3	3	65.50	57682.5659
G2361	20.10	0.15	0.213 ± 0.044	0.203	0.285 (+0.129/-0.089)	0.320	2.00 ± 0.50	3	3	65.10	58563.1065
G2385	18.60	0.15	0.652 ± 0.168	0.577	0.188 (+0.110/-0.069)	0.239	2.00 ± 0.50	11	10	77.94	57432.1497
G2474	18.40	0.15	0.558 ± 0.120	0.509	0.247 (+0.188/-0.107)	0.299	2.00 ± 0.50	0	5	73.46	58285.3802
G2687	19.00	0.15	0.537 ± 0.137	0.450	0.177 (+0.116/-0.070)	0.246	2.00 ± 0.50	4	4	84.67	58444.6468
G2882	18.70	0.15	0.613 ± 0.144	0.594	0.133 (+0.070/-0.046)	0.146	2.00 ± 0.50	4	4	61.12	58172.3197
G2911	19.20	0.15	0.392 ± 0.079	0.331	0.189 (+0.104/-0.067)	0.258	2.00 ± 0.50	5	5	83.60	57701.6729
G3081	18.40	0.15	0.537 ± 0.118	0.456	0.228 (+0.122/-0.079)	0.309	2.00 ± 0.50	7	7	82.97	58558.8293
G3243	16.50	0.15	1.362 ± 0.375	1.284	0.204 (+0.146/-0.085)	0.234	2.00 ± 0.50	9	9	67.51	58170.1108
I9173	18.90	0.15	1.222 ± 0.282	1.184	0.032 (+0.017/-0.011)	0.035	2.00 ± 0.50	4	4	61.11	58131.2692
J4268	18.20	0.15	2.362 ± 0.579	2.039	0.038 (+0.021/-0.013)	0.050	2.00 ± 0.50	2	3	81.08	57314.9369
J4386	16.90	0.15	2.329 ± 0.602	1.988	0.118 (+0.069/-0.043)	0.158	2.00 ± 0.50	3	2	82.38	57500.9009
K0754	18.60	0.15	0.496 ± 0.123	0.462	0.261 (+0.167/-0.102)	0.304	2.00 ± 0.50	0	8	69.59	57340.0457
K4131	19.80	0.15	0.225 ± 0.057	0.189	0.303 (+0.194/-0.118)	0.417	2.00 ± 0.50	1	1	84.10	57006.3744
K4232	18.30	0.15	0.693 ± 0.117	0.638	0.310 (+0.115/-0.084)	0.369	2.00 ± 0.50	7	7	71.93	57345.2830
K8565	17.10	0.15	1.240 ± 0.371	1.216	0.166 (+0.121/-0.070)	0.177	2.00 ± 0.50	0	7	57.21	57453.5533
L5442	18.50	0.15	0.717 ± 0.198	0.700	0.150 (+0.094/-0.058)	0.161	2.00 ± 0.50	13	12	59.04	57599.9503
L9021	16.90	0.15	1.754 ± 0.547	1.686	0.141 (+0.102/-0.059)	0.156	2.00 ± 0.50	7	7	63.23	57537.7883
M0839	17.30	0.15	1.771 ± 0.525	1.724	0.122 (+0.083/-0.049)	0.132	2.00 ± 0.50	4	4	59.82	58257.9219
M0909	18.20	0.15	2.377 ± 0.719	2.194	0.042 (+0.030/-0.017)	0.050	2.00 ± 0.50	2	2	71.48	58008.2539
N5756	18.70	0.15	0.593 ± 0.135	0.537	0.193 (+0.098/-0.065)	0.236	2.00 ± 0.50	3	5	74.48	57130.4819
N9849	18.60	0.15	0.609 ± 0.116	0.564	0.308 (+0.140/-0.096)	0.363	2.00 ± 0.50	9	9	70.88	57709.5789
O2191	19.00	0.15	0.384 ± 0.104	0.329	0.294 (+0.180/-0.112)	0.394	2.00 ± 0.50	3	3	82.16	57217.3365
O2643	17.40	0.15	2.717 ± 0.831	2.382	0.027 (+0.019/-0.011)	0.035	2.00 ± 0.50	2	2	79.13	57236.6518
O2708	18.10	0.15	0.703 ± 0.167	0.610	0.179 (+0.119/-0.072)	0.234	2.00 ± 0.50	5	5	80.44	58244.4696
O4670	18.50	0.15	0.931 ± 0.232	0.902	0.121 (+0.068/-0.043)	0.132	2.00 ± 0.50	14	14	61.11	58623.4258
O7360	19.20	0.15	0.606 ± 0.174	0.566	0.100 (+0.116/-0.054)	0.117	2.00 ± 0.50	0	7	69.44	56873.8031
O8083	16.00	0.15	4.960 ± 1.446	4.960	0.047 (+0.032/-0.019)	0.048	2.00 ± 0.50	1	1	47.56	57759.6806
P0697	17.80	0.15	1.119 ± 0.339	0.976	0.152 (+0.106/-0.062)	0.197	2.00 ± 0.50	7	7	79.76	58590.4201
P1346	16.80	0.15	1.250 ± 0.256	1.093	0.229 (+0.103/-0.071)	0.296	2.00 ± 0.50	9	10	79.44	56708.3470
P2558	20.20	0.15	0.890 ± 0.211	0.816	0.041 (+0.022/-0.014)	0.049	2.00 ± 0.50	4	4	72.57	57806.9828
P9221	19.10	0.15	0.574 ± 0.158	0.531	0.148 (+0.093/-0.057)	0.175	2.00 ± 0.50	2	2	71.29	56738.1250
Q2623	18.60	0.15	0.543 ± 0.127	0.514	0.218 (+0.122/-0.078)	0.247	2.00 ± 0.50	0	11	66.62	58131.8596
Q5196	18.80	0.15	0.431 ± 0.103	0.381	0.267 (+0.143/-0.093)	0.340	2.00 ± 0.50	9	9	78.14	58133.2761
Q7223	18.10	0.15	1.156 ± 0.283	1.077	0.145 (+0.080/-0.052)	0.169	2.00 ± 0.50	3	3	69.92	57404.5682
R5974	18.50	0.15	0.587 ± 0.184	0.509	0.180 (+0.182/-0.091)	0.236	2.00 ± 0.50	2	2	80.41	57472.5974
R7142	16.70	0.15	1.117 ± 0.337	1.054	0.208 (+0.170/-0.094)	0.238	2.00 ± 0.50	1	1	67.45	57109.0293
R7475	20.10	0.15	0.306 ± 0.075	0.259	0.186 (+0.147/-0.082)	0.254	2.00 ± 0.50	3	3	83.69	56883.8944
R9816	19.10	0.15	0.461 ± 0.114	0.413	0.162 (+0.109/-0.065)	0.201	2.00 ± 0.50	7	7	76.21	58241.4700
S1365	17.40	0.15	0.976 ± 0.188	0.916	0.206 (+0.112/-0.073)	0.237	2.00 ± 0.50	6	6	68.42	58106.5563
S6079	19.20	0.15	0.449 ± 0.105	0.406	0.205 (+0.107/-0.070)	0.251	2.00 ± 0.50	4	4	74.87	56945.3829
U2311	19.40	0.15	0.374 ± 0.086	0.320	0.187 (+0.112/-0.070)	0.250	2.00 ± 0.50	2	2	81.97	58103.1528
U3250	18.10	0.15	0.592 ± 0.159	0.537	0.258 (+0.209/-0.115)	0.314	2.00 ± 0.50	4	4	74.39	57236.3529
U6383	21.50	0.15	0.135 ± 0.023	0.110	0.184 (+0.069/-0.050)	0.267	2.00 ± 0.50	2	2	87.50	58139.6795

Table 1:: Thermal model fits for manually recovered NEOs detected in the NEOWISE Reactivation survey data. Names are in MPC-packed format, H and G are the input photometric parameter measurements used by the model, p_V is the visible light albedo, and n_{W1} and n_{W2} are the numbers of detections in the W1 and W2 bandpasses. D_{corr} and $p_{V_{corr}}$ have been corrected following the equations in Mommert *et al.* (2018).

[†]Albedo uncertainties are symmetric in log-space as the error is dominated by the uncertainty on H ; the asymmetric linear equivalents of the 1σ log-space uncertainties are presented here.

Name	input H (mag)	G	Diameter (km)	D_{corr} (km)	p_V^{\dagger}	$p_{V_{corr}}$	beaming	n_{W1}	n_{W2}	phase (deg)	Mean MJD days
U6462	18.50	0.15	0.909 ± 0.195	0.894	0.204 (+0.140/-0.083)	0.216	2.00 ± 0.50	11	11	56.06	57031.9860
U8635	21.90	-0.12	0.339 ± 0.102	0.290	0.027 (+0.061/-0.019)	0.036	2.00 ± 0.50	3	3	82.30	57694.4485
V0560	17.80	0.15	0.852 ± 0.252	0.778	0.176 (+0.135/-0.077)	0.212	2.00 ± 0.50	5	5	73.42	58016.7090
V7255	19.80	0.15	0.406 ± 0.090	0.396	0.200 (+0.098/-0.066)	0.216	2.00 ± 0.50	4	4	59.44	57844.5278
V8411	17.10	0.15	1.112 ± 0.246	1.022	0.242 (+0.142/-0.089)	0.289	2.00 ± 0.50	9	9	72.23	58571.1116
V9988	19.50	0.15	0.423 ± 0.094	0.376	0.139 (+0.069/-0.046)	0.175	2.00 ± 0.50	5	7	77.06	57833.5004
W5102	20.10	0.15	0.269 ± 0.055	0.229	0.410 (+0.230/-0.147)	0.552	2.00 ± 0.50	7	9	82.51	57097.4579
W6388	18.30	0.15	2.027 ± 0.498	1.826	0.023 (+0.013/-0.008)	0.029	2.00 ± 0.50	3	3	75.37	58036.9963
W9770	17.90	0.15	0.952 ± 0.157	0.913	0.183 (+0.094/-0.062)	0.203	2.00 ± 0.50	13	13	63.72	57170.1513
X7228	15.40	0.15	3.443 ± 0.806	3.451	0.107 (+0.067/-0.041)	0.108	2.00 ± 0.50	1	1	45.67	58097.5589
Y4074	18.70	0.15	0.507 ± 0.118	0.463	0.223 (+0.115/-0.076)	0.269	2.00 ± 0.50	6	6	73.28	57726.7940
Y9074	18.30	0.15	1.782 ± 0.472	1.701	0.039 (+0.023/-0.014)	0.043	2.00 ± 0.50	6	6	64.97	57677.3633
Z0988	16.80	0.15	1.576 ± 0.524	1.560	0.143 (+0.111/-0.063)	0.150	2.00 ± 0.50	1	1	53.54	58186.3185
Z7024	19.50	0.15	0.397 ± 0.106	0.328	0.179 (+0.109/-0.068)	0.256	2.00 ± 0.50	8	8	86.21	57641.5206
Z7028	19.40	0.15	0.409 ± 0.098	0.389	0.183 (+0.109/-0.068)	0.207	2.00 ± 0.50	0	3	65.92	57708.8640
Z9369	18.50	0.15	0.741 ± 0.167	0.702	0.134 (+0.067/-0.045)	0.152	2.00 ± 0.50	5	5	66.51	57596.0220
a3599	21.00	0.15	0.197 ± 0.041	0.161	0.212 (+0.099/-0.067)	0.307	2.00 ± 0.50	1	1	87.17	58219.8183
a3831	19.20	0.15	0.443 ± 0.132	0.376	0.229 (+0.156/-0.093)	0.311	2.00 ± 0.50	4	4	83.19	57677.4248
a4877	17.30	0.15	1.801 ± 0.402	1.755	0.117 (+0.058/-0.039)	0.126	2.00 ± 0.50	5	5	59.53	58533.3694
a5246	15.90	0.15	3.472 ± 1.076	3.397	0.096 (+0.081/-0.044)	0.103	2.00 ± 0.50	8	9	58.13	56772.9552
a7684	18.20	0.15	0.930 ± 0.249	0.900	0.115 (+0.070/-0.044)	0.126	2.00 ± 0.50	5	6	61.45	58576.8986
a9264	16.30	0.15	1.957 ± 0.566	1.722	0.129 (+0.085/-0.051)	0.164	2.00 ± 0.50	14	14	78.64	57711.9925
a9264	16.30	0.15	1.856 ± 0.388	1.834	0.157 (+0.079/-0.053)	0.165	2.00 ± 0.50	3	3	54.36	57683.8577
b0702	17.40	0.15	1.410 ± 0.365	1.399	0.113 (+0.094/-0.051)	0.117	2.00 ± 0.50	1	1	52.55	57877.3592
b1336	17.40	0.15	1.171 ± 0.307	1.125	0.205 (+0.122/-0.076)	0.227	2.00 ± 0.50	7	7	63.44	58055.0627
b7097	19.60	0.15	0.376 ± 0.102	0.326	0.224 (+0.180/-0.100)	0.294	2.00 ± 0.50	4	4	80.61	56667.4645
c0981	18.70	0.15	0.496 ± 0.114	0.449	0.238 (+0.141/-0.088)	0.291	2.00 ± 0.50	0	1	74.77	57182.5795
c5252	19.30	0.15	0.360 ± 0.096	0.315	0.260 (+0.179/-0.106)	0.335	2.00 ± 0.50	0	10	79.15	56720.9055
c5843	20.50	0.15	0.343 ± 0.079	0.305	0.095 (+0.057/-0.036)	0.120	2.00 ± 0.50	0	5	77.47	56681.5244
c7668	20.40	0.15	0.285 ± 0.087	0.244	0.150 (+0.106/-0.062)	0.202	2.00 ± 0.50	0	1	82.45	56732.0267
c7793	16.50	0.15	1.836 ± 0.402	1.774	0.122 (+0.059/-0.040)	0.133	2.00 ± 0.50	6	6	61.94	56934.4322
c9694	18.10	0.15	0.749 ± 0.204	0.657	0.177 (+0.127/-0.074)	0.228	2.00 ± 0.50	4	4	79.08	57321.7359
d1508	19.10	0.15	0.393 ± 0.099	0.369	0.239 (+0.135/-0.086)	0.275	2.00 ± 0.50	4	4	68.62	57852.2973
d7847	18.80	0.15	0.471 ± 0.105	0.411	0.226 (+0.188/-0.102)	0.292	2.00 ± 0.50	5	5	79.63	56805.0624
d8188	19.40	0.15	0.471 ± 0.127	0.451	0.188 (+0.115/-0.071)	0.210	2.00 ± 0.50	3	3	64.19	58341.4144
e1856	20.20	0.15	0.975 ± 0.226	0.874	0.016 (+0.014/-0.007)	0.020	2.00 ± 0.50	7	7	76.10	56786.8017
e5212	18.00	0.15	0.700 ± 0.186	0.679	0.267 (+0.213/-0.118)	0.290	2.00 ± 0.50	5	5	60.45	58274.6650
f3260	19.40	0.15	0.395 ± 0.090	0.347	0.196 (+0.123/-0.076)	0.251	2.00 ± 0.50	10	13	78.51	58365.5445
f4287	17.70	0.15	2.450 ± 0.698	2.199	0.122 (+0.079/-0.048)	0.151	2.00 ± 0.50	5	5	75.90	56929.1791
f7581	17.20	0.15	1.126 ± 0.238	1.041	0.145 (+0.068/-0.046)	0.171	2.00 ± 0.50	4	4	71.14	57795.1005
f7874	18.10	0.15	0.852 ± 0.210	0.812	0.156 (+0.096/-0.059)	0.175	2.00 ± 0.50	6	6	65.30	56997.7791
f8094	19.60	0.15	0.972 ± 0.228	0.837	0.054 (+0.028/-0.018)	0.071	2.00 ± 0.50	4	3	81.34	57909.3293
f8233	18.30	0.15	1.204 ± 0.290	1.118	0.181 (+0.098/-0.063)	0.212	2.00 ± 0.50	8	11	70.40	57069.7785
f8416	20.30	0.15	0.280 ± 0.071	0.245	0.171 (+0.098/-0.062)	0.221	2.00 ± 0.50	0	3	79.41	56858.8357
f8929	17.00	0.15	1.809 ± 0.491	1.703	0.102 (+0.063/-0.039)	0.117	2.00 ± 0.50	1	1	67.91	58439.6598
f9880	19.50	0.15	0.965 ± 0.281	0.918	0.040 (+0.026/-0.016)	0.045	2.00 ± 0.50	2	2	65.85	58510.1131

Table 1:: Thermal model fits for manually recovered NEOs detected in the NEOWISE Reactivation survey data. Names are in MPC-packed format, H and G are the input photometric parameter measurements used by the model, p_V is the visible light albedo, and n_{W1} and n_{W2} are the numbers of detections in the W1 and W2 bandpasses. D_{corr} and $p_{V_{corr}}$ have been corrected following the equations in Mommert *et al.* (2018).

[†]Albedo uncertainties are symmetric in log-space as the error is dominated by the uncertainty on H ; the asymmetric linear equivalents of the 1σ log-space uncertainties are presented here.

Name	input H (mag)	G	Diameter (km)	D_{corr} (km)	p_V^{\dagger}	$p_{V_{corr}}$	beaming	n_{W1}	n_{W2}	phase (deg)	Mean MJD days
g0591	19.30	0.15	0.360 ± 0.088	0.313	0.277 (+0.163/-0.103)	0.361	2.00 ± 0.50	6	6	80.04	57702.7559
g4965	18.80	0.15	0.632 ± 0.167	0.565	0.160 (+0.096/-0.060)	0.199	2.00 ± 0.50	11	12	76.38	57064.3201
g9094	20.10	0.15	0.311 ± 0.074	0.263	0.209 (+0.150/-0.088)	0.285	2.00 ± 0.50	8	8	83.23	57116.3349
h1107	17.70	0.15	2.108 ± 0.494	2.098	0.033 (+0.020/-0.012)	0.034	2.00 ± 0.50	0	3	50.79	57198.4014
h3953	20.70	0.15	0.332 ± 0.103	0.270	0.074 (+0.053/-0.031)	0.108	2.00 ± 0.50	3	3	87.55	57705.3136
h6037	18.60	0.15	0.683 ± 0.211	0.645	0.159 (+0.191/-0.087)	0.182	2.00 ± 0.50	5	5	67.43	57020.8262
h6325	18.40	0.15	0.709 ± 0.171	0.664	0.157 (+0.085/-0.055)	0.182	2.00 ± 0.50	3	3	68.77	58140.3297
h6329	20.10	0.15	1.238 ± 0.293	1.128	0.053 (+0.028/-0.018)	0.064	2.00 ± 0.50	7	7	73.70	57147.8066
h6724	19.90	0.15	0.422 ± 0.113	0.341	0.096 (+0.074/-0.042)	0.142	2.00 ± 0.50	2	4	88.32	57231.4184
h6775	16.50	0.15	1.372 ± 0.393	1.224	0.180 (+0.122/-0.073)	0.226	2.00 ± 0.50	2	2	76.84	57134.9233
h8661	19.40	0.15	0.331 ± 0.081	0.278	0.297 (+0.194/-0.117)	0.411	2.00 ± 0.50	5	6	84.37	57425.7596
h9877	19.50	0.15	0.613 ± 0.107	0.527	0.085 (+0.032/-0.023)	0.113	2.00 ± 0.50	5	6	81.66	57177.2392
i4004	20.50	0.15	0.343 ± 0.111	0.298	0.117 (+0.136/-0.063)	0.152	2.00 ± 0.50	7	8	80.37	56696.6192
i4193	18.10	0.15	0.722 ± 0.152	0.615	0.197 (+0.096/-0.064)	0.266	2.00 ± 0.50	4	4	82.76	58221.0599
i6924	20.20	0.15	0.328 ± 0.073	0.304	0.191 (+0.095/-0.063)	0.225	2.00 ± 0.50	5	5	70.74	57367.5552
j0142	19.90	0.15	0.297 ± 0.064	0.254	0.339 (+0.198/-0.125)	0.454	2.00 ± 0.50	4	4	82.02	57343.1318
j0160	16.70	0.15	1.898 ± 0.527	1.823	0.119 (+0.075/-0.046)	0.132	2.00 ± 0.50	5	5	63.43	57470.2564
j0263	18.80	0.15	0.765 ± 0.160	0.674	0.191 (+0.088/-0.060)	0.243	2.00 ± 0.50	7	7	78.52	57411.3131
j0649	19.50	0.15	0.343 ± 0.087	0.295	0.217 (+0.123/-0.079)	0.287	2.00 ± 0.50	5	7	81.35	57300.8436
j0894	18.30	0.15	0.898 ± 0.227	0.770	0.119 (+0.076/-0.046)	0.159	2.00 ± 0.50	1	1	81.89	58220.2739
j2302	20.40	0.15	0.837 ± 0.259	0.683	0.021 (+0.019/-0.010)	0.031	2.00 ± 0.50	1	1	87.37	57378.9721
j2376	20.00	0.15	0.292 ± 0.063	0.251	0.301 (+0.153/-0.101)	0.401	2.00 ± 0.50	4	4	81.59	57389.8650
j3563	20.20	0.15	0.210 ± 0.042	0.177	0.300 (+0.182/-0.113)	0.412	2.00 ± 0.50	7	7	83.89	57378.4104
j4094	21.90	0.15	0.157 ± 0.052	0.133	0.132 (+0.126/-0.064)	0.180	2.00 ± 0.50	5	5	83.69	56694.1089
j5554	18.00	0.15	2.064 ± 0.525	1.831	0.037 (+0.021/-0.013)	0.047	2.00 ± 0.50	3	3	77.49	57393.9945
k2775	19.40	0.15	1.391 ± 0.432	1.314	0.016 (+0.026/-0.010)	0.018	2.00 ± 0.50	1	1	67.31	57654.5868
k4797	18.30	0.15	1.047 ± 0.270	0.975	0.103 (+0.060/-0.038)	0.120	2.00 ± 0.50	4	4	69.80	57601.2832
k5824	21.70	0.15	0.242 ± 0.053	0.223	0.076 (+0.037/-0.025)	0.091	2.00 ± 0.50	6	6	72.18	57469.1084
k6508	18.60	0.15	0.822 ± 0.257	0.721	0.108 (+0.078/-0.045)	0.138	2.00 ± 0.50	10	10	78.95	56771.4604
k7309	19.90	0.15	0.169 ± 0.042	0.153	0.365 (+0.206/-0.132)	0.448	2.00 ± 0.50	2	2	74.90	58289.2730
k7336	20.50	0.15	0.237 ± 0.051	0.218	0.234 (+0.112/-0.076)	0.278	2.00 ± 0.50	5	5	72.00	57568.5081
k7963	18.60	0.15	0.673 ± 0.163	0.595	0.278 (+0.164/-0.103)	0.354	2.00 ± 0.50	5	5	78.07	57674.1217
k8583	17.90	0.15	0.800 ± 0.175	0.671	0.171 (+0.083/-0.056)	0.236	2.00 ± 0.50	4	5	84.40	57707.6874
l1240	21.70	0.15	0.119 ± 0.024	0.097	0.283 (+0.175/-0.108)	0.414	2.00 ± 0.50	3	4	87.77	57649.1891
l1241	18.20	0.15	2.598 ± 0.714	2.251	0.064 (+0.040/-0.025)	0.084	2.00 ± 0.50	4	4	80.59	57603.1260
l1323	19.40	0.15	1.312 ± 0.323	1.263	0.060 (+0.033/-0.022)	0.067	2.00 ± 0.50	6	7	62.92	57570.9236
l1956	19.20	0.15	0.430 ± 0.110	0.406	0.304 (+0.175/-0.111)	0.346	2.00 ± 0.50	6	6	66.88	57353.6623
l5534	21.30	0.15	0.194 ± 0.059	0.154	0.124 (+0.088/-0.051)	0.188	2.00 ± 0.50	1	1	89.74	58419.8649
l7162	20.60	0.15	0.263 ± 0.065	0.226	0.160 (+0.108/-0.065)	0.213	2.00 ± 0.50	2	2	81.71	57629.7126
l7327	18.30	0.15	1.061 ± 0.317	0.921	0.117 (+0.080/-0.048)	0.153	2.00 ± 0.50	5	5	80.31	57713.7312
m0004	17.20	0.15	2.077 ± 0.360	1.979	0.125 (+0.064/-0.042)	0.140	2.00 ± 0.50	11	11	65.29	57718.9329
m0823	20.10	0.15	0.254 ± 0.054	0.217	0.248 (+0.153/-0.095)	0.332	2.00 ± 0.50	2	2	82.02	57753.6418
m2488	19.70	0.15	0.301 ± 0.076	0.255	0.257 (+0.194/-0.111)	0.350	2.00 ± 0.50	0	2	83.30	57490.6980
m3563	18.70	0.15	0.639 ± 0.127	0.621	0.180 (+0.079/-0.055)	0.195	2.00 ± 0.50	8	8	60.38	57809.0954
m6739	19.60	0.15	0.395 ± 0.108	0.338	0.188 (+0.117/-0.072)	0.252	2.00 ± 0.50	1	1	82.17	57755.7736
m8450	17.20	0.15	1.357 ± 0.419	1.327	0.127 (+0.090/-0.053)	0.135	2.00 ± 0.50	0	2	58.14	57860.9007

Table 1:: Thermal model fits for manually recovered NEOs detected in the NEOWISE Reactivation survey data. Names are in MPC-packed format, H and G are the input photometric parameter measurements used by the model, p_V is the visible light albedo, and n_{W1} and n_{W2} are the numbers of detections in the W1 and W2 bandpasses. D_{corr} and $p_{V_{corr}}$ have been corrected following the equations in Mommert *et al.* (2018).

[†]Albedo uncertainties are symmetric in log-space as the error is dominated by the uncertainty on H ; the asymmetric linear equivalents of the 1σ log-space uncertainties are presented here.

Name	input H (mag)	G	Diameter (km)	D_{corr} (km)	p_V^{\dagger}	$p_{V_{corr}}$	beaming	n_{W1}	n_{W2}	phase (deg)	Mean MJD days
n5323	19.60	0.15	0.968 ± 0.214	0.897	0.040 (+0.020/-0.013)	0.047	2.00 ± 0.50	8	8	70.93	56834.5034
n5829	18.70	0.15	0.793 ± 0.190	0.780	0.091 (+0.090/-0.045)	0.097	2.00 ± 0.50	3	4	56.43	58322.3134
n6817	19.90	0.15	0.287 ± 0.077	0.248	0.160 (+0.125/-0.070)	0.211	2.00 ± 0.50	4	4	80.92	58022.1404
n6861	18.00	0.15	0.857 ± 0.237	0.825	0.137 (+0.086/-0.053)	0.151	2.00 ± 0.50	6	6	62.67	57994.1245
n7117	18.30	0.15	0.856 ± 0.230	0.813	0.239 (+0.155/-0.094)	0.270	2.00 ± 0.50	6	5	66.22	58171.3180
n8548	20.00	0.15	0.273 ± 0.063	0.251	0.245 (+0.146/-0.091)	0.291	2.00 ± 0.50	6	6	71.93	58058.6083
o1647	22.30	0.15	0.128 ± 0.029	0.107	0.154 (+0.082/-0.053)	0.214	2.00 ± 0.50	4	4	84.54	56884.2964
o4680	19.80	0.15	0.340 ± 0.104	0.323	0.174 (+0.180/-0.088)	0.196	2.00 ± 0.50	6	6	66.12	58096.2616
o4800	21.80	0.15	0.550 ± 0.166	0.464	0.020 (+0.016/-0.009)	0.028	2.00 ± 0.50	5	5	83.64	58366.5793
o8772	19.80	0.15	0.277 ± 0.067	0.239	0.337 (+0.211/-0.130)	0.446	2.00 ± 0.50	3	3	81.40	58046.9496
o8912	19.50	0.15	0.289 ± 0.062	0.255	0.337 (+0.207/-0.128)	0.429	2.00 ± 0.50	4	4	78.11	58171.2531
o8918	19.20	0.15	0.618 ± 0.199	0.571	0.115 (+0.086/-0.049)	0.136	2.00 ± 0.50	8	8	71.50	57066.4452
o9520	18.90	0.15	0.667 ± 0.132	0.631	0.146 (+0.067/-0.046)	0.166	2.00 ± 0.50	5	5	67.03	58202.2393
o9523	19.30	0.15	1.469 ± 0.422	1.374	0.023 (+0.015/-0.009)	0.027	2.00 ± 0.50	2	2	69.09	58100.3090
p1137	19.00	0.15	0.597 ± 0.171	0.529	0.178 (+0.175/-0.088)	0.225	2.00 ± 0.50	5	5	77.83	56822.5975
p1684	20.70	0.15	0.191 ± 0.047	0.175	0.174 (+0.121/-0.071)	0.209	2.00 ± 0.50	1	1	73.22	58158.8102
p2245	19.90	0.15	0.316 ± 0.075	0.269	0.250 (+0.151/-0.094)	0.337	2.00 ± 0.50	3	3	82.53	58088.7794
p3550	17.20	0.15	2.057 ± 0.780	2.012	0.064 (+0.064/-0.032)	0.069	2.00 ± 0.50	1	1	58.18	56813.8657
p5010	18.90	0.15	0.570 ± 0.114	0.518	0.170 (+0.082/-0.055)	0.207	2.00 ± 0.50	7	7	74.11	58233.6185
p5049	19.30	0.15	0.523 ± 0.148	0.496	0.114 (+0.103/-0.054)	0.129	2.00 ± 0.50	4	4	66.44	58217.8786
p6155	20.20	0.15	0.255 ± 0.059	0.221	0.238 (+0.175/-0.101)	0.312	2.00 ± 0.50	2	2	80.63	57479.3443
p8507	19.80	0.15	0.416 ± 0.128	0.375	0.123 (+0.186/-0.074)	0.151	2.00 ± 0.50	0	7	75.32	58002.9813
p8640	20.10	0.15	0.277 ± 0.063	0.247	0.200 (+0.101/-0.067)	0.252	2.00 ± 0.50	5	5	77.10	58379.2253
q0808	20.10	0.15	0.965 ± 0.262	0.882	0.027 (+0.021/-0.012)	0.032	2.00 ± 0.50	2	3	73.12	57670.8571
q2684	21.10	0.15	0.140 ± 0.037	0.122	0.275 (+0.173/-0.106)	0.355	2.00 ± 0.50	3	3	79.56	58232.2785
q2684	21.10	0.15	0.149 ± 0.027	0.140	0.352 (+0.136/-0.098)	0.407	2.00 ± 0.50	5	5	68.98	57873.9345
q3586	22.10	0.15	0.120 ± 0.036	0.099	0.164 (+0.163/-0.082)	0.236	2.00 ± 0.50	2	2	86.64	58248.6678
q3625	19.60	0.15	1.251 ± 0.244	1.121	0.040 (+0.017/-0.012)	0.049	2.00 ± 0.50	4	4	76.15	58178.0271
q3775	19.00	0.15	0.441 ± 0.098	0.389	0.220 (+0.128/-0.081)	0.281	2.00 ± 0.50	4	4	78.38	57090.8911
q3806	17.40	0.15	2.558 ± 0.674	2.555	0.030 (+0.022/-0.013)	0.030	2.00 ± 0.50	0	1	48.58	58452.0661
q3815	17.50	0.15	1.083 ± 0.213	1.041	0.185 (+0.111/-0.069)	0.205	2.00 ± 0.50	4	5	63.40	58384.7499
q3915	18.20	0.15	0.887 ± 0.249	0.845	0.231 (+0.147/-0.090)	0.259	2.00 ± 0.50	5	5	65.29	57011.3303
q4459	20.10	0.15	0.299 ± 0.078	0.289	0.203 (+0.120/-0.075)	0.223	2.00 ± 0.50	9	9	62.01	58597.9761
q4530	19.50	0.15	0.371 ± 0.099	0.325	0.219 (+0.134/-0.083)	0.282	2.00 ± 0.50	1	1	79.15	58448.2261
q5477	19.10	0.15	0.439 ± 0.103	0.367	0.183 (+0.096/-0.063)	0.254	2.00 ± 0.50	2	2	84.68	58568.6464
q8284	21.20	0.15	0.305 ± 0.081	0.288	0.064 (+0.039/-0.024)	0.073	2.00 ± 0.50	5	6	67.66	58521.8291
q9450	19.30	0.15	0.657 ± 0.176	0.573	0.174 (+0.144/-0.079)	0.226	2.00 ± 0.50	2	3	79.75	58431.7027
q9951	21.00	0.15	0.304 ± 0.082	0.285	0.096 (+0.073/-0.042)	0.111	2.00 ± 0.50	3	3	68.60	57850.8881
J99T16T	19.60	0.15	0.978 ± 0.210	0.849	0.052 (+0.025/-0.017)	0.069	2.00 ± 0.50	4	4	80.39	57322.7342
K07D41L	20.70	0.15	0.201 ± 0.050	0.166	0.245 (+0.137/-0.088)	0.351	2.00 ± 0.50	3	3	86.53	56928.7337
K07M06K	20.30	0.15	0.264 ± 0.063	0.235	0.201 (+0.138/-0.082)	0.253	2.00 ± 0.50	2	2	77.01	57555.8048
K08G04A	19.10	0.15	0.458 ± 0.109	0.409	0.290 (+0.157/-0.102)	0.362	2.00 ± 0.50	4	4	76.70	57086.9705
K08H01Z	19.20	0.15	0.747 ± 0.233	0.700	0.071 (+0.051/-0.030)	0.082	2.00 ± 0.50	3	3	68.80	58632.8547
K08J30Y	18.90	0.15	0.573 ± 0.112	0.535	0.165 (+0.096/-0.061)	0.192	2.00 ± 0.50	3	3	69.71	57380.9110
K08O02V	20.30	0.15	0.294 ± 0.065	0.255	0.155 (+0.109/-0.064)	0.204	2.00 ± 0.50	0	7	80.55	58633.3114
K08P09R	22.50	0.15	0.113 ± 0.027	0.093	0.138 (+0.129/-0.067)	0.197	2.00 ± 0.50	0	2	86.45	57507.9383

Table 1:: Thermal model fits for manually recovered NEOs detected in the NEOWISE Reactivation survey data. Names are in MPC-packed format, H and G are the input photometric parameter measurements used by the model, p_V is the visible light albedo, and n_{W1} and n_{W2} are the numbers of detections in the W1 and W2 bandpasses. D_{corr} and $p_{V_{corr}}$ have been corrected following the equations in Mommert *et al.* (2018).

[†]Albedo uncertainties are symmetric in log-space as the error is dominated by the uncertainty on H ; the asymmetric linear equivalents of the 1σ log-space uncertainties are presented here.

Name	input H (mag)	G	Diameter (km)	D_{corr} (km)	p_V^{\dagger}	$p_{V_{corr}}$	beaming	n_{W1}	n_{W2}	phase (deg)	Mean MJD days
K08S00D	19.40	0.15	0.489 ± 0.123	0.441	0.122 (+0.069/-0.044)	0.151	2.00 ± 0.50	4	4	75.47	57803.7806
K08W00L	21.70	0.15	0.697 ± 0.205	0.643	0.038 (+0.026/-0.015)	0.045	2.00 ± 0.50	3	2	71.62	58078.4608
K09D46L	22.00	0.15	0.121 ± 0.025	0.107	0.266 (+0.123/-0.084)	0.339	2.00 ± 0.50	5	5	78.43	57525.8599
K09U00G	23.30	0.15	0.168 ± 0.042	0.136	0.049 (+0.028/-0.018)	0.072	2.00 ± 0.50	1	1	88.15	57658.5908
K14J25O	17.80	0.15	0.732 ± 0.174	0.660	0.177 (+0.143/-0.079)	0.217	2.00 ± 0.50	3	3	75.22	56779.2826
K16Y08C	24.60	0.15	0.045 ± 0.011	0.041	0.127 (+0.093/-0.054)	0.155	2.00 ± 0.50	0	2	75.08	57769.3487
K17A04M	19.10	0.15	0.373 ± 0.078	0.331	0.347 (+0.181/-0.119)	0.439	2.00 ± 0.50	12	13	77.57	56861.5611
K17A05F	17.70	0.15	1.596 ± 0.349	1.525	0.078 (+0.038/-0.025)	0.087	2.00 ± 0.50	6	6	64.66	57750.9725
K17A19P	23.60	0.15	0.049 ± 0.012	0.039	0.289 (+0.185/-0.113)	0.436	2.00 ± 0.50	1	1	89.50	57761.8081
K17B03M	23.00	0.15	0.106 ± 0.034	0.095	0.119 (+0.113/-0.058)	0.147	2.00 ± 0.50	2	2	75.35	57794.2338
K17B05P	20.30	0.15	0.343 ± 0.073	0.321	0.134 (+0.067/-0.045)	0.156	2.00 ± 0.50	3	3	69.44	57735.8117
K17B06Q	21.40	0.15	0.120 ± 0.027	0.103	0.130 (+0.103/-0.057)	0.172	2.00 ± 0.50	1	1	81.29	57791.2648
K17B31M	20.70	0.15	0.216 ± 0.062	0.191	0.165 (+0.159/-0.081)	0.210	2.00 ± 0.50	4	4	78.34	57937.3490
K17B31P	19.80	0.15	0.795 ± 0.242	0.704	0.034 (+0.035/-0.017)	0.042	2.00 ± 0.50	3	3	77.76	57808.4781
K17C00S	19.80	0.15	1.011 ± 0.266	0.922	0.032 (+0.019/-0.012)	0.038	2.00 ± 0.50	1	2	73.36	57901.3026
K17C00S	19.80	0.15	0.916 ± 0.256	0.874	0.056 (+0.036/-0.022)	0.062	2.00 ± 0.50	15	14	65.02	57874.4810
K17C31X	25.10	0.15	0.039 ± 0.010	0.035	0.133 (+0.075/-0.048)	0.166	2.00 ± 0.50	2	2	76.35	57787.8763
K17D34T	27.80	0.15	0.018 ± 0.005	0.014	0.043 (+0.047/-0.022)	0.064	2.00 ± 0.50	0	1	88.95	57808.5727
K17D34W	23.20	0.15	0.078 ± 0.021	0.064	0.151 (+0.095/-0.058)	0.219	2.00 ± 0.50	0	1	87.31	57816.2267
K17D36C	22.10	0.15	0.183 ± 0.056	0.145	0.036 (+0.039/-0.019)	0.054	2.00 ± 0.50	1	1	90.37	57801.9627
K17E00K	24.10	0.15	0.040 ± 0.010	0.032	0.254 (+0.140/-0.090)	0.385	2.00 ± 0.50	1	1	89.70	57827.6906
K17E02S	19.40	0.15	0.653 ± 0.176	0.553	0.113 (+0.070/-0.043)	0.154	2.00 ± 0.50	1	1	83.26	57863.9265
K17E04L	25.40	0.15	0.055 ± 0.020	0.044	0.041 (+0.071/-0.026)	0.061	2.00 ± 0.50	0	1	88.70	57817.0770
K17E13Q	19.90	0.15	0.353 ± 0.093	0.300	0.137 (+0.114/-0.062)	0.186	2.00 ± 0.50	3	3	82.86	57857.8568
K17E13R	21.50	0.15	0.137 ± 0.036	0.114	0.333 (+0.221/-0.133)	0.470	2.00 ± 0.50	4	4	85.70	57786.4710
K17H01C	20.80	0.15	0.376 ± 0.086	0.351	0.073 (+0.061/-0.033)	0.085	2.00 ± 0.50	2	2	69.56	57876.7530
K17H49P	22.90	0.15	0.118 ± 0.040	0.098	0.087 (+0.088/-0.044)	0.124	2.00 ± 0.50	0	4	86.09	57904.1436
K17K27R	23.50	0.15	0.057 ± 0.010	0.051	0.352 (+0.237/-0.141)	0.435	2.00 ± 0.50	1	1	75.74	57908.9956
K17M01B	18.80	0.15	0.491 ± 0.146	0.407	0.213 (+0.146/-0.086)	0.301	2.00 ± 0.50	1	1	85.73	57955.8959
K17M05B	22.60	0.15	0.108 ± 0.031	0.088	0.181 (+0.120/-0.072)	0.265	2.00 ± 0.50	3	3	87.89	57944.4070
K17N05S	20.70	0.15	0.588 ± 0.164	0.551	0.033 (+0.022/-0.013)	0.038	2.00 ± 0.50	6	6	68.59	57591.1684
K17P26L	22.20	0.15	0.174 ± 0.048	0.152	0.140 (+0.088/-0.054)	0.182	2.00 ± 0.50	4	5	79.75	57989.6921
K17Q18M	18.60	0.15	0.845 ± 0.266	0.840	0.090 (+0.160/-0.058)	0.093	2.00 ± 0.50	0	11	51.66	57917.7248
K17R00L	18.50	0.15	0.670 ± 0.196	0.579	0.187 (+0.153/-0.084)	0.246	2.00 ± 0.50	24	26	80.78	57981.8972
K17S14T	23.50	0.15	0.110 ± 0.028	0.095	0.067 (+0.141/-0.045)	0.088	2.00 ± 0.50	1	1	80.67	58029.8567
K17S17R	18.80	0.15	1.027 ± 0.243	0.975	0.067 (+0.036/-0.023)	0.076	2.00 ± 0.50	4	4	66.17	58048.5511
K17T04A	19.40	0.15	0.890 ± 0.281	0.739	0.039 (+0.061/-0.024)	0.055	2.00 ± 0.50	0	1	85.40	58025.5076
K17U00O	20.20	0.15	0.338 ± 0.080	0.290	0.136 (+0.089/-0.054)	0.181	2.00 ± 0.50	1	1	81.86	58037.0736
K17U02P	20.00	0.15	0.380 ± 0.082	0.347	0.266 (+0.136/-0.090)	0.321	2.00 ± 0.50	6	6	73.46	58043.7040
K17U03C	22.70	0.15	0.143 ± 0.046	0.117	0.075 (+0.057/-0.032)	0.109	2.00 ± 0.50	1	1	87.44	58049.8568
K17V14U	18.60	0.15	0.543 ± 0.152	0.485	0.192 (+0.230/-0.105)	0.240	2.00 ± 0.50	2	2	76.73	58133.9417
K17V15L	21.20	0.15	0.277 ± 0.070	0.252	0.077 (+0.044/-0.028)	0.094	2.00 ± 0.50	6	6	74.07	58229.7254
K17W01S	20.20	0.15	0.364 ± 0.111	0.319	0.133 (+0.094/-0.055)	0.172	2.00 ± 0.50	7	7	79.36	58103.7583
K17W13F	18.10	0.15	2.405 ± 0.808	2.326	0.056 (+0.044/-0.025)	0.061	2.00 ± 0.50	7	7	61.57	58044.1060
K17W13V	21.10	0.15	0.249 ± 0.058	0.239	0.104 (+0.111/-0.054)	0.115	2.00 ± 0.50	0	3	63.45	58099.9237
K17W14H	18.00	0.15	0.738 ± 0.172	0.682	0.156 (+0.081/-0.054)	0.185	2.00 ± 0.50	5	5	71.38	58221.1926

Table 1:: Thermal model fits for manually recovered NEOs detected in the NEOWISE Reactivation survey data. Names are in MPC-packed format, H and G are the input photometric parameter measurements used by the model, p_V is the visible light albedo, and n_{W1} and n_{W2} are the numbers of detections in the W1 and W2 bandpasses. D_{corr} and $p_{V_{corr}}$ have been corrected following the equations in Mommert *et al.* (2018).

[†]Albedo uncertainties are symmetric in log-space as the error is dominated by the uncertainty on H ; the asymmetric linear equivalents of the 1σ log-space uncertainties are presented here.

Name	input H (mag)	G	Diameter (km)	D_{corr} (km)	p_V^{\dagger}	$p_{V_{corr}}$	beaming	n_{W1}	n_{W2}	phase (deg)	Mean MJD days
K17W14K	21.70	0.15	0.172 ± 0.046	0.165	0.124 (+0.139/-0.066)	0.139	2.00 ± 0.50	0	4	65.00	58078.5803
K17X02O	22.40	0.15	0.147 ± 0.039	0.136	0.101 (+0.060/-0.038)	0.119	2.00 ± 0.50	2	2	71.52	58068.4959
K17Y01R	20.00	0.15	0.351 ± 0.099	0.332	0.152 (+0.098/-0.060)	0.173	2.00 ± 0.50	4	4	66.81	58120.6729
K17Y08S	19.50	0.15	0.784 ± 0.209	0.666	0.052 (+0.031/-0.020)	0.070	2.00 ± 0.50	5	5	82.99	58146.6197
K18A04E	24.70	0.15	0.096 ± 0.017	0.078	0.025 (+0.011/-0.008)	0.036	2.00 ± 0.50	1	1	87.51	58129.2398
K18B02Y	20.50	0.15	0.260 ± 0.064	0.244	0.216 (+0.119/-0.077)	0.249	2.00 ± 0.50	6	7	68.37	58209.4853
K18C02G	19.20	0.15	0.682 ± 0.183	0.635	0.084 (+0.091/-0.044)	0.098	2.00 ± 0.50	3	3	70.08	58161.2419
K18C02O	19.40	0.15	0.516 ± 0.141	0.451	0.099 (+0.063/-0.038)	0.128	2.00 ± 0.50	2	2	79.48	58184.8028
K18C02Z	21.40	0.15	0.272 ± 0.062	0.225	0.071 (+0.053/-0.030)	0.100	2.00 ± 0.50	1	1	85.88	58181.3388
K18C14B	21.30	0.15	0.223 ± 0.054	0.213	0.108 (+0.064/-0.040)	0.120	2.00 ± 0.50	0	4	63.83	58159.6126
K18E00E	21.70	0.15	0.188 ± 0.043	0.178	0.131 (+0.071/-0.046)	0.149	2.00 ± 0.50	5	5	67.12	58187.7701
K18J01E	19.90	0.15	0.375 ± 0.111	0.368	0.168 (+0.125/-0.072)	0.178	2.00 ± 0.50	5	5	56.72	58280.5585
K18L05F	20.20	0.15	0.310 ± 0.102	0.299	0.139 (+0.107/-0.060)	0.153	2.00 ± 0.50	20	19	62.55	58309.0224
K18L15Q	20.80	0.15	0.377 ± 0.082	0.334	0.166 (+0.081/-0.054)	0.210	2.00 ± 0.50	12	13	77.66	58309.5869
K18M06Y	21.20	0.15	0.669 ± 0.207	0.612	0.038 (+0.027/-0.016)	0.046	2.00 ± 0.50	11	12	72.91	58293.4605
K18M06Y	21.20	0.15	0.759 ± 0.182	0.676	0.040 (+0.022/-0.014)	0.050	2.00 ± 0.50	8	8	76.86	58281.9182
K18T04D	22.10	0.15	0.250 ± 0.061	0.208	0.048 (+0.026/-0.017)	0.067	2.00 ± 0.50	3	3	85.56	58561.3594
K18U01A	19.70	0.15	0.374 ± 0.087	0.336	0.162 (+0.084/-0.055)	0.201	2.00 ± 0.50	3	3	75.72	58407.8800
K18U01N	19.30	0.15	0.649 ± 0.178	0.642	0.096 (+0.076/-0.042)	0.101	2.00 ± 0.50	4	4	53.61	58446.8304
K18U02Q	21.90	0.15	0.273 ± 0.076	0.234	0.055 (+0.035/-0.021)	0.074	2.00 ± 0.50	2	2	81.81	58408.2443
K18V00X	21.10	0.15	0.168 ± 0.035	0.144	0.212 (+0.174/-0.096)	0.281	2.00 ± 0.50	1	1	81.40	58419.1726
K18W01R	20.30	0.15	0.458 ± 0.160	0.445	0.084 (+0.069/-0.038)	0.091	2.00 ± 0.50	3	3	60.52	58484.7210
K18X00R	18.50	0.15	0.710 ± 0.173	0.645	0.137 (+0.081/-0.051)	0.166	2.00 ± 0.50	1	1	74.03	58500.9948
K18X02Z	21.60	0.15	0.259 ± 0.071	0.234	0.196 (+0.123/-0.075)	0.241	2.00 ± 0.50	34	34	75.09	58493.9276
K19C02D	20.09	0.15	0.441 ± 0.127	0.377	0.082 (+0.067/-0.037)	0.110	2.00 ± 0.50	1	1	82.26	58518.3875
K19C02L	23.34	0.15	0.073 ± 0.018	0.063	0.179 (+0.099/-0.064)	0.234	2.00 ± 0.50	1	1	80.40	58558.8947
K19E00Q	19.36	0.15	0.473 ± 0.131	0.459	0.128 (+0.092/-0.054)	0.139	2.00 ± 0.50	7	7	60.65	58544.3332
K19F00D	23.32	0.15	0.215 ± 0.062	0.173	0.019 (+0.024/-0.011)	0.028	2.00 ± 0.50	1	1	88.69	58558.9033
K19J05U	24.00	0.15	0.056 ± 0.011	0.048	0.128 (+0.103/-0.057)	0.173	2.00 ± 0.50	3	3	82.75	58607.7321
K19N07D	21.43	0.15	0.198 ± 0.048	0.165	0.122 (+0.100/-0.055)	0.170	2.00 ± 0.50	0	2	84.82	58677.9404